crystals

MDPI

Article

The Influence of La and Ce on Thermal Conductivity of Magnesium Alloys

Wei He [1], Wenxin Hu [1,2,*], Bin Kang [3], Yuming Lu [1], Kun Li [1,2], Siyuan Qu [3], Feng Liu [1,2], Wei Wang [1], Yuan Li [4], Zhiguo Luo [5] and He Guo [1]

[1] Baotou Research Institute of Rare Earths, Baotou 014030, China; hewei@brire.com (W.H.); yuminglu@brire.com (Y.L.); likun@brire.com (K.L.); liufeng@brire.com (F.L.); 13664774273@163.com (W.W.); heguo@brire.com (H.G.)
[2] National Key Laboratory of Baiyunobo Rare Earth Resource Researches and Comprehensive Utilization, Baotou 014030, China
[3] Rare Earth Advanced Materials Technology Innovation Center, Inner Mongolia Northern Rare Earth Advanced Materials Technology Innovation Co., Ltd., Baotou 014030, China; kangbin@reamtic.cn (B.K.); qusiyuan@reamtic.cn (S.Q.)
[4] Baotou Metallurgical Building Research Institute, Baotou 014030, China; he13030462937@126.com
[5] School of Metallurgy, Northeastern University, Shenyang 110819, China; luozg@smm.neu.edu.cn
* Correspondence: wenxinhu@brire.com; Tel.: +86-15598419440

Abstract

With the development of science and technology, heat dissipation has become a bottleneck problem restricting the development of fields such as transportation, machinery, electronics, and aerospace. Aiming to resolve the bottleneck problem of low thermal conductivity in traditional commercial magnesium alloys, this paper designed alloy compositions to investigate the effects of the solid solubility of La and Ce, and the size, morphology, distribution, and volume fraction of the second phase in the microstructure of magnesium alloys during the heat dissipation performance of the Mg-RE binary system and the Mg-Mn-La(Ce) system. The research shows that through CAFE simulation calculations, regulation can be achieved via the following methods: increasing the average nucleation undercooling, which leads to larger grain sizes; reducing the nucleation density, which results in larger grain sizes; and increasing the standard deviation of the average nucleation undercooling, which reduces the area of small grains while increasing the area of large grains. The thermal conductivity of both as-cast and solid-solution Mg-La (Ce) binary alloys gradually decreases with the increase in the added elements. However, after solution treatment, the thermal conductivity of the Mg-La (Ce) binary alloys is higher than that of the as-cast alloys. The addition of the Ce element helps refine the as-cast microstructure of the Mg-0.5Mn alloy. With the increase in Ce addition, the volume fraction of the Mg12Ce phase also increases. The thermal conductivity of the as-cast Mg-0.5Mn-xCe alloy gradually increases with rising temperature. Meanwhile, at room temperature, the thermal conductivity of the as-cast Mg-0.5Mn alloy gradually decreases with the increase in Ce addition, and the rate of decline gradually slows down due to the precipitation of the Mg12Ce phase.

Keywords: magnesium alloy; heat dissipation; rare earth; mechanism

Check for updates

Academic Editor: Saif Haider Kayani

Received: 27 January 2026
Revised: 26 February 2026
Accepted: 26 February 2026
Published: 28 February 2026

Copyright: © 2026 by the authors. Licensee MDPI, Basel, Switzerland. This article is an open access article distributed under the terms and conditions of the Creative Commons Attribution (CC BY) license.

1. Introduction

With the development of science and technology, heat dissipation has become a bottleneck problem restricting the development of fields such as transportation, machinery,

electronics, and aerospace. Statistics show that up to 55% of failures in electronic components are caused by excessively high temperatures, making heat dissipation an important and urgent problem to resolve in the electronics industry [1–3]. For example, thermal management design is one of the most critical design tasks for LED lighting fixtures. Currently, the luminous efficiency of LEDs ranges from approximately 20% to 45%, with the majority of electrical energy converted into heat [4,5]. Due to heat concentration at the PN junction, inadequate heat dissipation causes the junction temperature of LEDs to rise rapidly. This accelerates the aging of surrounding materials such as phosphors, plastic mounts, and lenses, thereby shortening the lifespan of the lighting fixture. Additionally, with the rise in new energy vehicles, components like permanent magnet motor housings and battery compartments now demand higher thermal performance standards.

Currently, the main heat dissipation alloy materials include copper alloys, aluminum alloys, and magnesium alloys [6]. Among them, pure copper has the highest thermal conductivity of 397 W/(m·K); pure aluminum is 247 W/(m·K); and pure magnesium is 158 W/(m·K) [7]. Although the thermal conductivity of pure magnesium is as high as 158 W/(m·K), the yield strength and tensile strength of as-cast pure magnesium are only 2.5 MPa and 11.5 MPa, respectively. Even for wrought pure magnesium, the yield strength and tensile strength are only 9.0 MPa and 20.0 MPa [8]. Such yield and tensile strengths cannot meet the mechanical property requirements for magnesium alloy materials. Therefore, it is necessary to improve the mechanical properties of magnesium alloys through methods such as alloying and composite strengthening. However, according to heat conduction theory, adding alloying elements to the matrix, whether forming solid solutions or second phases, will significantly reduce the material's thermal conductivity. The factors affecting the thermal conductivity of magnesium alloys are complex. From a microscopic perspective, any factor affecting electron and phonon scattering will influence the thermal conductivity of magnesium alloys [9–11]. The purer the metal, the higher its thermal and electrical conductivity. Adding any alloying element will deteriorate the thermal conductivity of pure magnesium to varying degrees. Due to differences in atomic volume, valence, solid solubility in Mg, and electron distribution outside the nucleus, different alloying atoms have varying degrees of influence on the thermal conductivity of pure magnesium [12]. The greater the difference in atomic radius between the alloying element and magnesium, the greater the degree of lattice distortion caused, and the lower the thermal conductivity.

Mg-Mn alloys, as early-developed commercial wrought magnesium alloys, exhibit excellent extrudability and superior corrosion resistance, and this series offers moderate strength [13]. The Mg-Mn system of magnesium alloys provides a study system for achieving a balance between thermal conductivity and mechanical properties. Rare earth elements can enhance the mechanical properties of magnesium alloys through grain refinement strengthening, second-phase strengthening, solution strengthening, and precipitation strengthening [14,15]. The atomic radius of common alloying elements and their solubility in magnesium alloys are shown in Table 1.

Research on the influence of alloying elements, including rare earth elements, on the thermal conductivity of magnesium alloys has made progress, and studies on rare-earth-element-containing Mg-Mn alloys have also been conducted. However, no reports have been published on the mechanisms by which rare earth element contents and solid solution concentrations affect the thermal conductivity of Mg-Mn alloys, nor on the selection mechanism for the equilibrium point between mechanical and thermal properties under solid-solution aging heat-treatment conditions.

Table 1. Atomic radius of common alloying elements and their solid solubility in magnesium alloys.

Atomic Number	Alloying Element	Atomic Radius/Å	Solid Solubility in Mg/at.%
12	Mg	1.602	-
13	Al	1.428	11.59 (437 °C)
20	Ca	1.970	0.82 (516 °C)
25	Mn	1.790	1.00 (659 °C)
30	Zn	1.530	2.40 (325 °C)
40	Zr	1.600	1.04 (654 °C)
50	Sn	1.510	3.35 (551 °C)
39	Y	1.803	3.35 (565 °C)
57	La	1.877	0.14 (613 °C)
58	Ce	1.824	0.09 (592 °C)
60	Nd	1.821	0.63 (548 °C)
62	Sm	1.804	0.99 (542 °C)
64	Gd	1.883	4.35 (548 °C)
66	Dy	1.781	4.83 (561 °C)
68	Er	1.761	6.90 (584 °C)

This paper selects La and Ce rare earth elements, which have low solid solubility in the magnesium matrix, have an atomic radius not too different from magnesium, and possess strengthening functions for the magnesium matrix, to study the effects of the solid solubility of La and Ce, and the size, morphology, distribution, and volume fraction of the second phase in the magnesium alloy microstructure during the heat dissipation performance of the Mg-RE binary system and the Mg-Mn-La(Ce) system. For the design of Mg-RE-Mn alloys based on thermodynamic equilibrium phase diagrams, we investigate lattice distortion caused by differences in the solid solubility of rare earth elements. The crystal structure, morphology, size, and volume fraction of rare-earth second phases formed within grains and at grain boundaries were investigated. The effects of reduced heterogeneous solute atoms within grains during aging and the common-plane defects caused by the coherent relationship between the second phase and the magnesium matrix interface on the thermal conductivity of magnesium alloys were examined. This work reveals the mechanism by which rare earth elements influence the thermal conductivity of magnesium alloys. It clarifies the principles governing how solution treatment and aging conditions influence the thermal conductivity of magnesium alloys and defines the selection mechanism for the equilibrium point between mechanical and thermal properties in magnesium alloys under heat treatment conditions.

2. Study on Heat Dissipation Properties of Mg-La(Ce) Binary Alloys

2.1. Phase Diagram Study of Mg-La(Ce) Alloys

The rare earth elements La and Ce exhibit low solid solubility in Mg. Using the thermodynamic calculation software Pandat_2021, the phase diagrams for Mg-La(Ce) alloys were computed. As shown in Figure 1 for the binary phase diagrams, the magnesium-rich end of the phase diagram was specifically examined to investigate the effects of La and Ce on the alloy phase diagrams [16].

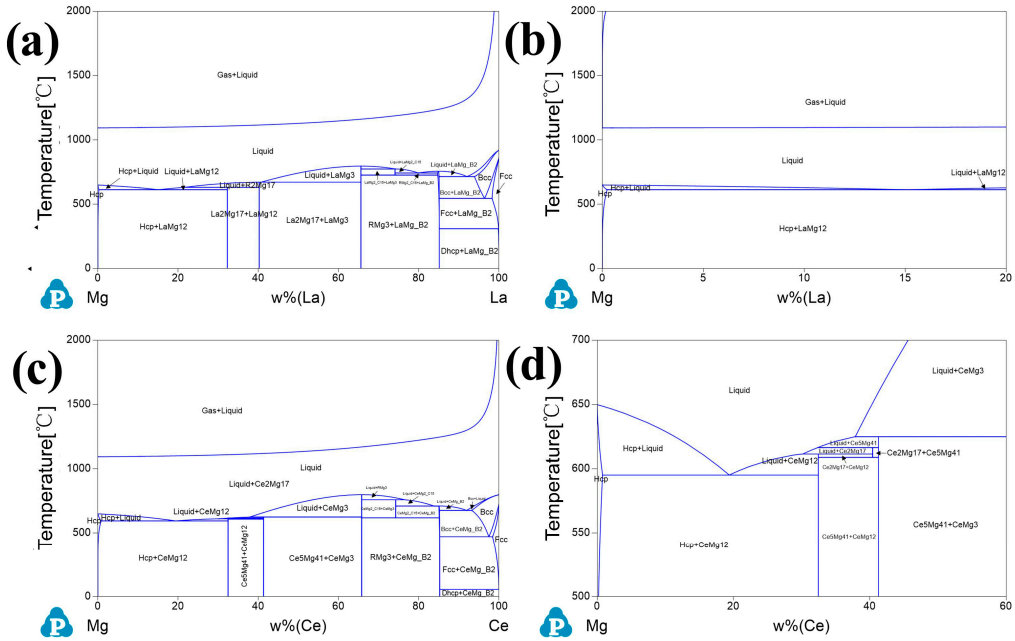


Figure 1. Phase diagram of Mg-La(Ce) binary alloy (**a**) Mg-La binary alloy phase diagram; (**b**) Mg-La binary alloy phase diagram at the Mg-rich end; (**c**) Mg-Ce binary alloy phase diagram; (**d**) Mg-Ce binary alloy phase diagram at the Mg-rich end.

2.2. Regulating the Microstructure of Alloys Through CAFE Calculations

(1) Model Equations

Mass Conservation Equation:

$$\frac{\partial \rho}{\partial t} + \nabla \cdot \left(\rho \vec{v} \right) = S_{\mathrm{m}} \tag{1}$$

Energy Conservation Equation:

$$\frac{\partial}{\partial t}\left(\rho \vec{v} \right) + \nabla \cdot \left(\rho \vec{v} \vec{v} \right) = \nabla \cdot \left(\mu grand \vec{v} \right) + S_{\mathrm{V}} \tag{2}$$

Heterogeneous Nucleation Grain Density Equation:

$$\frac{dn}{d(\Delta T)} = \frac{n_{\max}}{\sqrt{2\pi}\Delta T_{\sigma}} \exp\left[-\frac{(\Delta T - \Delta T_{\max})^2}{2\Delta T_{\sigma}^2} \right] \tag{3}$$

Dendrite Tip Growth Kinetic Equation:

$$\Delta \mathrm{T} = \Delta T_c + \Delta T_t + \Delta T_k + \Delta T_r \tag{4}$$

In the equation, ρ is density; t is time; $\vec{v}$ is the velocity vector; S_{m} is the source of quality; S_{V} is the generalized source term of the momentum conservation equation; $n_{\max}$ is the maximum nuclear density, m^{-3}; ΔT_{σ} is the standard deviation of nucleation undercooling, °C; $\Delta T_{\max}$ is the average nucleation undercooling, °C; ΔT_c is the degree of undercooling of the components, °C; ΔT_c is the degree of undercooling of the thermodynamics, °C; ΔT_r is the degree of undercooling of the solid–liquid interface curvature, °C; ΔT_k is the degree of undercooling of the Growth Dynamics, °C [17,18].

(2) Determination of Simulation Parameters

To investigate the effects of volume-averaged nucleation undercooling, nucleation density, and the standard deviation of nucleation undercooling on alloy microstructure,

simulations were conducted using different values of $\Delta T_{v,\max}$, $\Delta T_{v,\sigma}$, and $n_{v,\max}$. The simulation parameters are listed in Table 2. The pouring temperature and mold temperature were set at 720 °C and 200 °C, respectively. Air cooling conditions were applied around the mold and on the top surface of the casting. The convective heat transfer coefficient h_1 = 100 W·m^{-2}·K^{-1} and the interfacial heat transfer coefficient between the mold and casting h_2 = 3000 W·m^{-2}·K^{-1} were adopted, which closely matched the experimental conditions.

Table 2. Nucleation parameters.

	$\Delta T_{v,\max}$ (°C)	$\Delta T_{v,\sigma}$ (°C)	$n_{v,\max}$ (1/cm^3)
(**a**)	10	1	2×10^{13}
(**b**)	30	1	2×10^{13}
(**c**)	70	1	2×10^{13}
(**d**)	10	1	2×10^{11}
(**e**)	10	1	2×10^{15}
(**f**)	10	20	2×10^{13}
(**g**)	10	100	2×10^{13}
(**h**)	10	200	2×10^{13}

(3) Model Validation

The model validation process employed Mg-5La as the experimental material, comparing the grain size calculated by the established CAFE model with the experimentally measured grain size to verify the model. When the average nucleation undercooling is 30 K, nucleation density is 2×10^{13} m^{-3}, and the standard deviation of nucleation undercooling is 1 K, the calculated solidification microstructure of the specimen is shown in Figure 2a. The solidification microstructure of the ingot simulated by ProCAST^{TM} 2021 Packages software consists almost entirely of fine equiaxed grains, with an average grain size of approximately 32.25 μm, as statistically determined by the software. A specimen of approximately 10 mm thick was extracted from the middle section of the casting. The as-cast microstructure is shown in Figure 2b. Under slow cooling conditions, the alloy's as-cast microstructure consists almost entirely of equiaxed grains. Statistical analysis of grain sizes at different locations indicates an average grain size of approximately 29.76 μm. The experimentally obtained as-cast microstructure is essentially consistent with the simulated results.

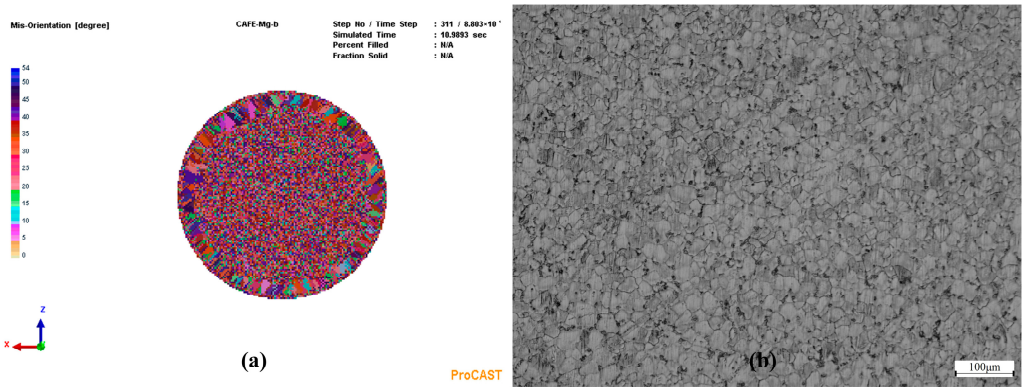


Figure 2. Microstructure diagram of Mg-5.0La alloy: (**a**) simulated microstructure of Mg-5.0La alloy; (**b**) experimental metallographic microstructure of the alloy.

(4) Optimal Parameters for the CAFE Model

During solidification, as temperature decreases, when the undercooling at the solidification front reaches the necessary nucleation undercooling, particles with strong nucleation

ability become the first nucleation nuclei. These nuclei continuously grow, thereby completing the transformation process from a liquid to a solid phase. As the degree of undercooling increases further, more heterogeneous particles become activated as nucleation nuclei, inhibiting continued grain growth. Thus, both grain formation and growth processes jointly control grain size.

The simulated microstructure of the casting is shown in Figure 3, where different colors represent distinct grain orientations. The figure reveals a thin layer of fine equiaxed grains forming along the mold wall at the outermost region of the casting. The supercooling required for heterogeneous nucleation is denoted by $\Delta T_{v,\max}$, and the number of heterogeneous nucleation particles is denoted by $n_{v,\max}$. During nucleation, when the required supercooling is reached, the particle is activated to initiate nucleation and growth. Thus, both factors jointly determine the number of heterogeneous particles capable of growth. As shown in a, b, and c, when other parameters remain constant, increasing the average nucleation undercooling leads to larger grain sizes. This indicates that the required undercooling for nucleation increases, reducing the number of activated nucleation sites and consequently increasing grain size. As shown in a, d, and e, grain size increases with decreasing nucleation density. Since fewer heterogeneous nuclei form, this effectively increases the required undercooling for nucleation. Under identical cooling conditions, fewer heterogeneous nuclei undergo nucleation and growth, leading to larger grain sizes. As shown in a, f, g, and h, when other parameters remain constant, increasing leads to larger grain sizes. This primarily controls the distribution of grain regions. As the standard deviation of the average nucleation undercooling increases, the area occupied by small grains decreases while that of large grains increases.

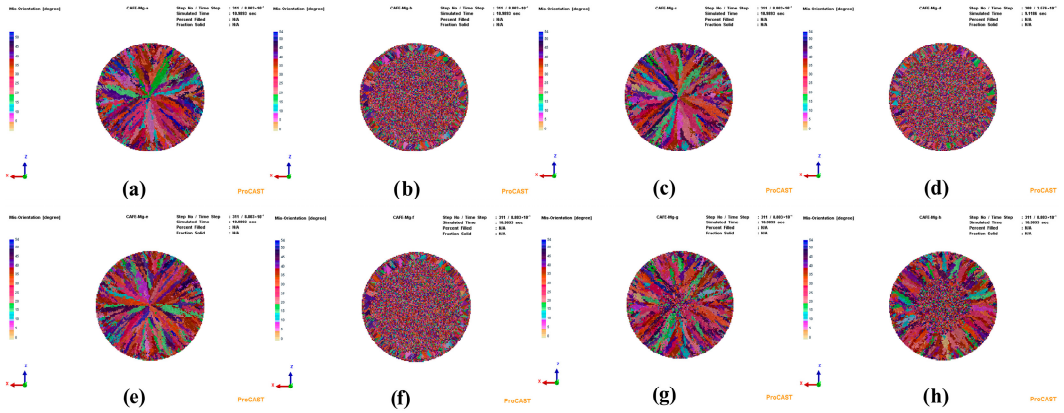


Figure 3. Casting solidification microstructure of (**a**–**h**).

Microstructure significantly influences the thermal conductivity of alloy materials. Both solid solution atoms and alloy second phases can affect the movement of alloy phonons and electrons, thereby reducing thermal conductivity. Therefore, simulating the microstructure of alloys to determine the effects of solidification process parameters on microstructure provides a reference for obtaining high thermal conductivity during subsequent alloy solidification.

2.3. Experimental Materials and Methods

The raw materials used for the experimental alloy were high-purity magnesium (99.98% by mass), Mg-25 wt.%La intermediate alloy, and Mg-25 wt.%Ce intermediate alloy. Prior to alloy melting, the mass ratios of various raw materials were calculated, accounting for combustion losses, with a 95% yield rate for the Mg-25 wt.%Ce element.

The specific alloy melting process is as follows:

(1) Preheated magnesium ingots (temperature exceeding 150 °C) were loaded into a preheated 60 kW resistance furnace. Melting proceeded under a mixed atmosphere shield (0.5 vol.% SF6 + 99.5 vol.% N2). The temperature was raised to 720 °C to melt the magnesium ingots while simultaneously preheating the iron casting mold to 200 °C.

(2) After complete melting of the magnesium ingots, the temperature was raised to 740 °C and magnesium–lanthanum, and magnesium–cerium intermediate alloys were added. Once fully melted, the mixture was stirred for 90 min and left to stand for 60 min. Slag removal was then initiated, followed by holding at 720 °C for 30 min.

(3) After powering off the resistance furnace, the furnace temperature dropped to 680–700 °C. The molten alloy was poured into custom iron molds and air-cooled to room temperature. Actual compositions of the four Mg-RE binary alloys were analyzed using X-ray fluorescence spectroscopy (XRF–1800CCDE). Design and actual compositions are shown in Table 3. The four as-cast binary magnesium alloys underwent heat treatment according to the specific solution treatment processes detailed in Table 3. Chemical composition analysis of the alloy involves sampling from five different locations on the specimens. After sampling, the samples are combined, and the average value is determined for analysis. Specimens were immediately water-quenched upon removal from the resistance furnace.

Table 3. Chemical composition of Mg-RE binary alloy and its heat treatment process.

Nominal Alloys	Compositions/wt.% (at.%)			Solid Solution Treatment
	La	Ce	Mg	
Mg-0.2La	0.20 (0.19)	-	Bal.	500 °C × 24 h
Mg-0.4La	0.40 (0.40)	-	Bal.	
Mg-0.6La	0.60 (0.57)	-	Bal.	
Mg-1.0La	1.00 (0.97)	-	Bal.	
Mg-1.5La	1.50 (1.44)	-	Bal.	
Mg-2.5La	2.50 (2.43)	-	Bal.	
Mg-3.5La	3.50 (3.34)	-	Bal.	
Mg-5.0La	5.00 (4.81)	-	Bal.	
Mg-0.2Ce	-	0.20 (0.20)	Bal.	500 °C × 24 h
Mg-0.4Ce	-	0.40 (0.38)	Bal.	
Mg-0.6Ce	-	0.60 (0.58)	Bal.	
Mg-1.0Ce	-	1.00 (1.02)	Bal.	
Mg-1.5Ce	-	1.50 (1.52)	Bal.	
Mg-2.5Ce	-	2.50 (2.22)	Bal.	
Mg-3.5Ce	-	3.50 (3.42)	Bal.	
Mg-5.0Ce	-	5.00 (5.38)	Bal.	

In this study, the laser flash method was used to test the thermal diffusivity of the as-cast and solid-solution binary alloys. The specimen size was a disc of 12.7 mm in diameter and 3 mm in thickness. The testing instrument was NETZSCH LFA 457 (Bavaria, Germany). Testing temperatures were 25 °C, 50 °C, 100 °C, 150 °C, and 200 °C. Each specimen was tested at least three times at different temperatures. The density of the specimens at room temperature was measured by the Archimedes method. In this paper, the specific heat

capacity of the binary alloys was calculated using the Neumann–Kopp rule. The thermal conductivity of the specimens was calculated from thermal diffusivity, density, and specific heat capacity using the following formulas:

$$\lambda = \alpha \cdot \rho \cdot C_p \quad (5)$$

$$\rho(T) = \rho_0 - 0.156(T - 25) \quad (6)$$

$$C_p = \sum(C_{pi} W_i) \quad (7)$$

In the equation, λ is thermal conductivity of materials, W/(m·°C); α is the thermal diffusivity coefficient, $mm^2 \cdot s^{-1}$; ρ_0 is the density of the sample at 25 °C, g/cm^3; T is the test temperature for thermal conductivity, °C; C_{pi} represents the specific heats of the alloying elements; W_i represents the mass percentage of the alloying element in the alloy.

Equipment utilized in this study:

(1) Simulation computing apparatus:

Thermodynamic calculation software Pandat_2021, casting process simulation software ProCAST^{TM} 2021 Packages, and simulation computing server.

(2) Heat treatment apparatus:

MXQ1200-50 (Tianjin Zhonghuan Electric Furnace Co., Ltd., Tianjin, China) Atmosphere-Controlled Heat Treatment Furnace

(3) Primary Testing and Analytical Equipment:

Composition Testing: ICPS-8100 High-Resolution Inductively Coupled Plasma Spectrometer (Shimadzu, Kyoto, Japan); X-ray Energy-Dispersive Spectrometer (Bruker, Karlsruhe, Germany).

Microstructural Analysis and Characterization Equipment: Axio Scope 5 Optical Microscope (Zeiss, Oberkochen, Baden-Württemberg, Germany), Sigma500 Field Emission Scanning Electron Microscope (Zeiss, Oberkochen, Baden-Württemberg, Germany), Bruker Energy-Dispersive Spectrometer, and X-ray Diffractometer (Panalytical, Almelo, The Netherlands).

Thermal Performance Evaluation Equipment: LFA 427 Laser Flux Profiler (NETZSCH, Bavaria, Germany), High-Precision Physical Balance.

2.4. Microstructure and Thermal Conductivity of Mg-(La)Ce Alloys

(1) Mg-La Alloys

After corrosion, the grains of as-cast Mg-1.5La, Mg-2.5La, and Mg-3.5La alloys are macroscopically visible to the naked eye. The metallographic photos of the Mg-La binary alloy are shown in Figure 4. The La content has a certain influence on the grain size, grain morphology, volume fraction of the second phase, and precipitation location of the as-cast Mg-La alloy.

From the optical microstructural photos of the as-cast Mg-xLa shown in Figure 4, it can be seen that in Mg-0.2La, the second-phase precipitates in granular form inside the grains, with a small amount of precipitation. In Mg-0.6La, the second-phase precipitates in elongated and granular forms inside the grains, and the orientation of the arranged second phases differs between adjacent grains. In Mg-1.0La, the precipitation location of the second phase is still inside the grains, but the arrangement orientation of the elongated second phases within the same grain is more random compared to Mg-0.6La. When the La content reaches 1.5 wt.%, the grain size significantly decreases to about 38 μm, and the precipitation location of the second phase shifts to grain boundaries. When the La content continues to increase (>1.5 wt.%), the grains continue to refine, but the grain refinement effect is

not as pronounced as that from Mg-0.2La → Mg-0.6La → Mg-1.5La. The solidification microstructure appears as dendrites + equiaxed grains. La plays a role in grain refinement for as-cast magnesium alloys. With the increase in La, the precipitation location of the second phase changes from intragranular to grain boundaries, and the volume fraction of the second phase increases.

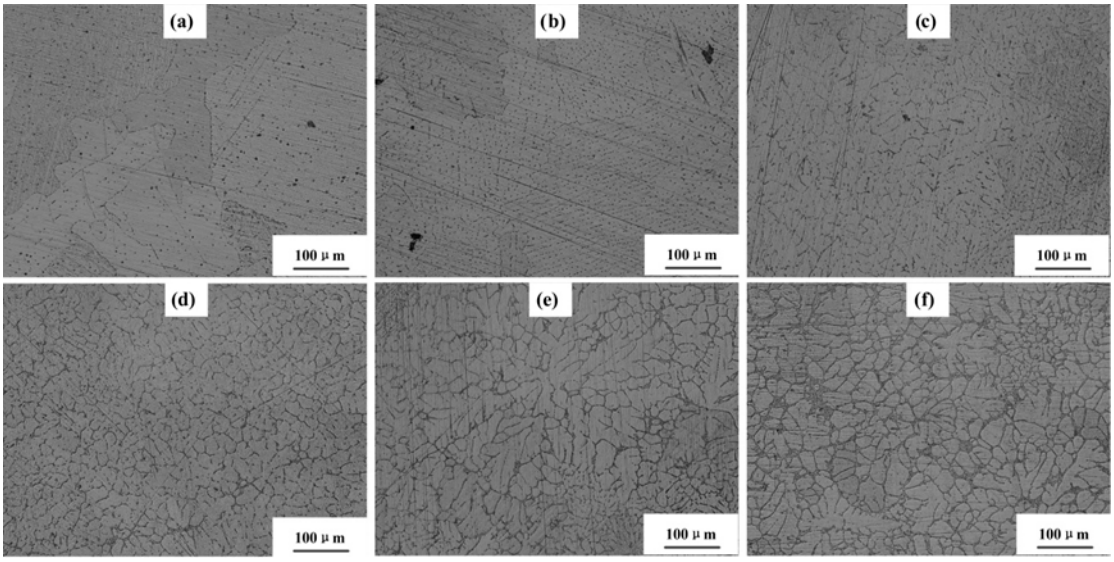


Figure 4. As-cast optical microstructure of Mg-La binary alloy. (**a**) Mg-0.2La; (**b**) Mg-0.6La; (**c**) Mg-1.0La; (**d**) Mg-1.5La; (**e**) Mg-2.5La; (**f**) Mg-3.5La.

Back-scattered electron (BSE) imaging utilizes high-energy elastic electrons to detect atomic number contrast. During scanning analysis, regions with higher atomic numbers on the sample surface collect more backscattered electrons, resulting in brighter images on the fluorescent screen. Conversely, regions with lower atomic numbers collect fewer backscattered electrons, producing darker images. Thus, areas containing heavier elements appear relatively brighter in the image, while regions with lighter elements appear relatively darker. The backscattered electron image reflects atomic number contrast. The atomic numbers of Mg and La are 12 and 57, respectively. Therefore, for a binary Mg-La alloy, regions containing more La appear brighter in the image.

The BSE scanning images of as-cast Mg-0.4La, Mg-1.0La, Mg-2.5La, and Mg-5.0La binary alloys are shown in Figure 5a–d. By applying noise reduction and binarization using Image Pro Plus 7.0 to define the grayscale extraction range, the volume fraction of the second phase can be analyzed and measured in BSE scans of as-cast Mg-0.4La, Mg-1.0La, Mg-2.5La, and Mg-5.0La binary alloys. These images reveal the microstructure of the alloys, including the α-Mg matrix and intermetallic compounds. In the as-cast Mg-0.4La and Mg-1.0La alloys, the secondary phase is distributed within grains and along grain boundaries. In contrast, the Mg-2.5La and Mg-5.0La alloys exhibit a semi-continuous and continuous network distribution of the secondary phase within the magnesium matrix. Analysis of the images enabled measurement of the volume fraction of the second phase in each alloy, which were 0.78%, 5.25%, 7.54%, and 10.21%, respectively. Furthermore, Figure 5e–h show BSE scanning microstructures of the solution-treated Mg-0.4La, Mg-1.0La, Mg-2.5La, and Mg-5.0La binary alloys; the images revealed no significant change in the amount of the second phase. Following solution treatment, the semi-continuous and continuous network compounds in the as-cast alloys transformed into fine, dispersed particles distributed throughout the magnesium matrix. In the solution-treated alloys, the volume fractions of the second phase were 0.80%, 5.32%, 7.66%, and 10.25%, respectively.

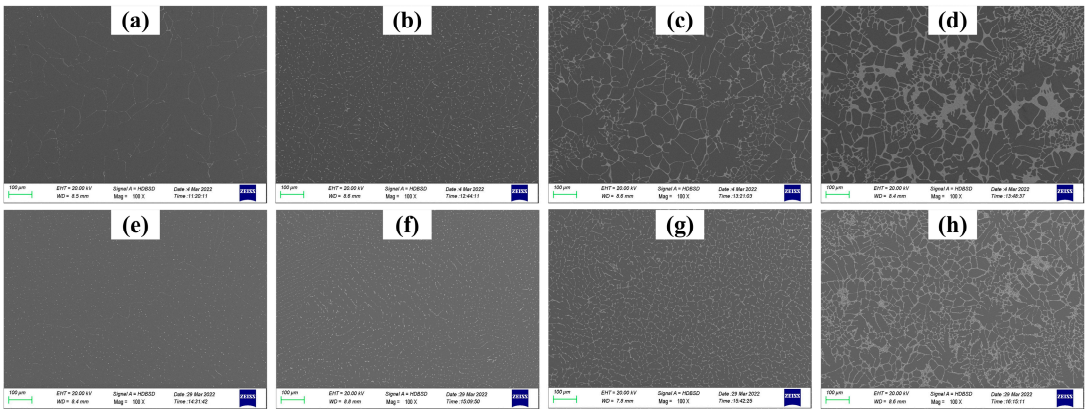


Figure 5. BSE scanning images of Mg-La binary alloy: (**a**–**d**) as-cast Mg-0.4La, Mg-1.0La, Mg-2.5La, and Mg-5.0La; (**e**–**h**) solution-treated Mg-0.4La, Mg-1.0La, Mg-2.5La, and Mg-5.0La.

EDS energy-dispersive spectroscopy analysis was performed on Mg-5.0La, and the results are shown in Figure 6. Based on the energy spectrum results at point A, the second phase in the Mg-La alloy was preliminarily identified as the $Mg_{12}La$ phase.

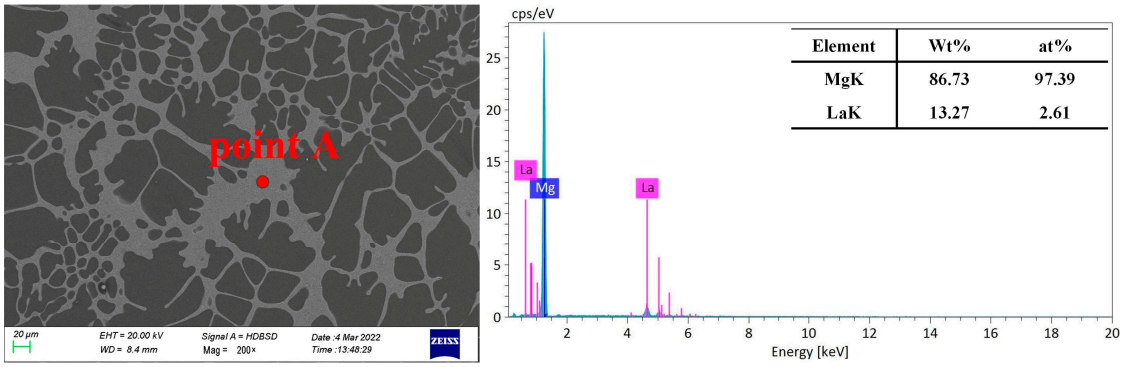


Figure 6. Energy spectrum analysis of as-cast Mg-5.0La.

Thermal physical properties are key performance indicators for developing magnesium alloys with high thermal conductivity. The purer the metal, the better its thermal conductivity. Thus, pure magnesium exhibits the highest thermal conductivity at 157 W/m·K, but its mechanical properties are too low, with a yield strength of only 20 MPa. Magnesium alloys with high thermal conductivity must maintain high mechanical properties while ensuring thermal conductivity exceeds 120 W/m·K. The influence of alloying elements on magnesium alloy thermal conductivity manifests in several ways: Alloying solid-solved elements in the α-Mg matrix introduces additional lattice defects, increasing electron and phonon scattering, and reducing their mean free path. When the alloying element content exceeds maximum solubility, secondary phases form with varying morphologies and distributions. The impacts on thermal conductivity, from greatest to least significant, are as follows: solid solution atoms > network-type secondary phases > granular dispersed secondary phases. As previously noted, Mg-La binary alloys primarily consist of an α-Mg matrix and $Mg_{12}La$ eutectic secondary phases.

The thermal conductivities of as-cast and solution-treated Mg-La binary alloys at room temperature are shown in Figure 7. As seen in the figure, both as-cast and solution-treated Mg-La binary alloys exhibit a gradual decrease in thermal conductivity with increasing La content. As the La content increases from 0.2 wt.% to 5.0 wt.%, the thermal conductivity of the cast Mg-0.2La alloy decreases from 144.1 W/(m·K) to 110.4 W/(m·K) for the Mg-5.0La alloy. Concurrently, the thermal conductivity of the solution-treated Mg-0.2La alloy

decreased from 151.8 W/(m·K) to 114.3 W/(m·K) for the Mg-5.0La alloy. Notably, the thermal conductivity of the solution-treated Mg-La binary alloy was higher than that of the corresponding cast Mg-La binary alloy.

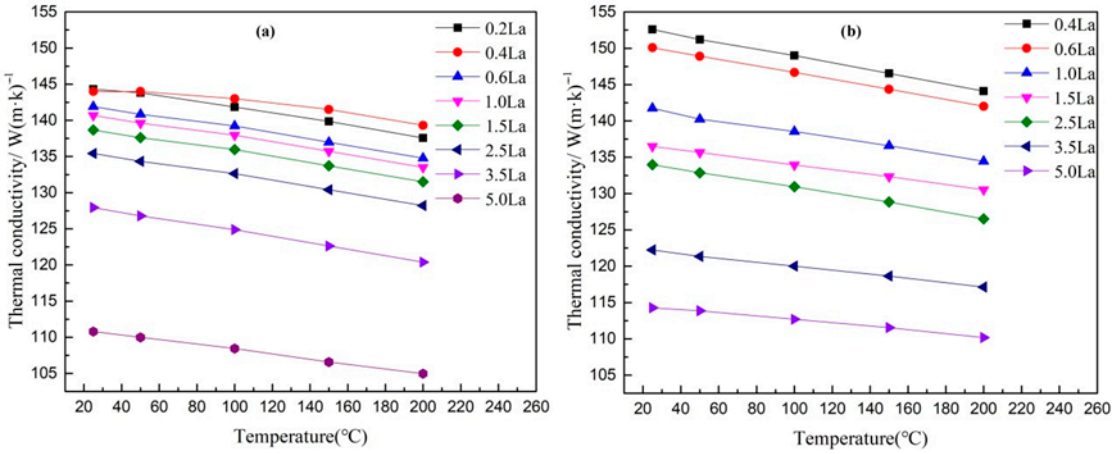


Figure 7. Thermal conductivity versus temperature curves of Mg-La alloy: (**a**) as-cast and (**b**) solution-treated alloy.

(2) Mg-Ce Alloys

The optical microscopic morphology of the as-cast Mg-xCe structure after corrosion is shown in Figure 8. In Mg-0.2Ce, the second-phase precipitates as granular structures within grains, with a relatively low amount of precipitation. In Mg-0.6Ce, the second-phase precipitates are elongated and granular structures within grains, and there are variations in orientation between adjacent grains. In Mg-1.0Ce, the second phase still precipitates within grains, but the orientation of elongated second-phase structures within the same grain is more random compared to Mg-0.6Ce.

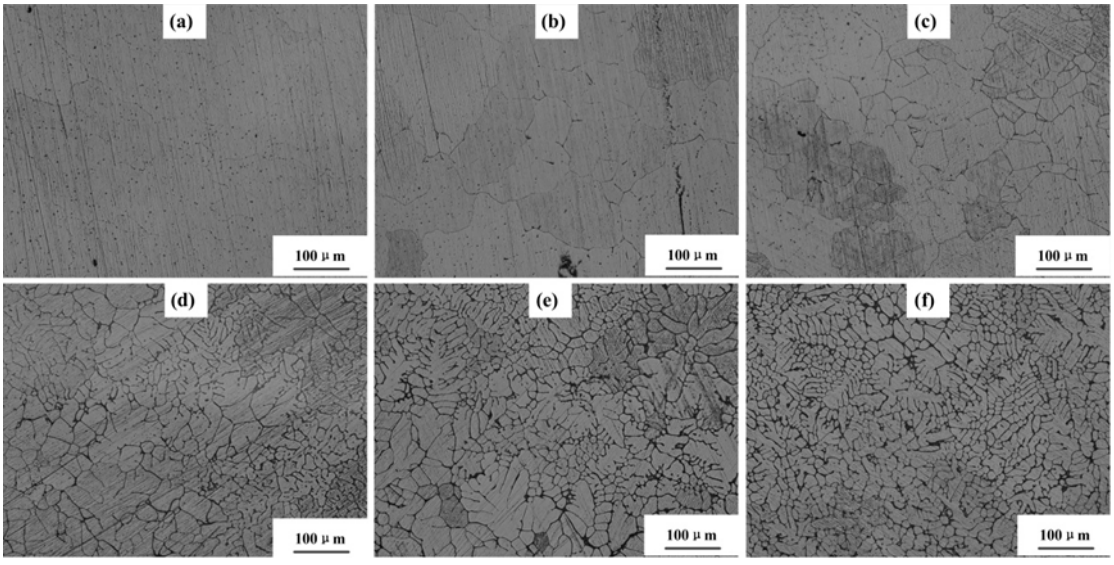


Figure 8. Optical microstructure of as-cast Mg-Ce binary alloy. (**a**) Mg-0.2Ce; (**b**) Mg-0.6Ce; (**c**) Mg-1.0Ce; (**d**) Mg-2.5Ce; (**e**) Mg-3.5Ce; (**f**) Mg-5.0Ce.

When the Ce content reaches 2.5 wt.%, the grain size significantly decreases to approximately 45 μm, and the precipitation location of the second phase shifts to grain boundaries. As Ce content further increases (>2.5 wt.%), grain refinement continues. However, beyond this point, the refinement effect becomes less pronounced compared to the

progression Mg-0.2Ce→Mg-0.6Ce→Mg-2.5Ce. The solidified microstructure exhibits a dendritic + equiaxed grain morphology. Ce exhibits a more pronounced grain refinement effect on as-cast magnesium alloys compared to La. Furthermore, as Ce content increases, the precipitation location of the second phase shifts from within grains to grain boundaries, and the volume fraction of the second phase increases.

Figure 9a–c show the BSE scanning microstructures of as-cast Mg-0.4Ce, Mg-1.0Ce, Mg-2.5Ce, and Mg-5.0Ce alloys. The microstructure of the as-cast alloys consists of an α-Mg matrix and some intermetallic compounds, with the volume fraction of intermetallic compounds in the alloy gradually increasing with the rising Ce content. For the as-cast Mg-0.4Ce alloy (Figure 4a), the second phase is dispersed within grains and along grain boundaries. In contrast, the second phase in the as-cast Mg-1.0Ce, Mg-2.5Ce, and Mg-5.0Ce alloys exhibits a semi-continuous and continuous network distribution within the magnesium matrix. BSE microstructures of the Mg-0.4Ce, Mg-1.0Ce, Mg-2.5Ce, and Mg-5.0Ce alloys after solution treatment are shown in Figure 9d–f. The figures reveal that the semi-continuous and continuous network compounds in the as-cast Mg-0.6Ce and Mg-1.5Ce alloys transform into finely dispersed particles distributed throughout the magnesium matrix after solution treatment.

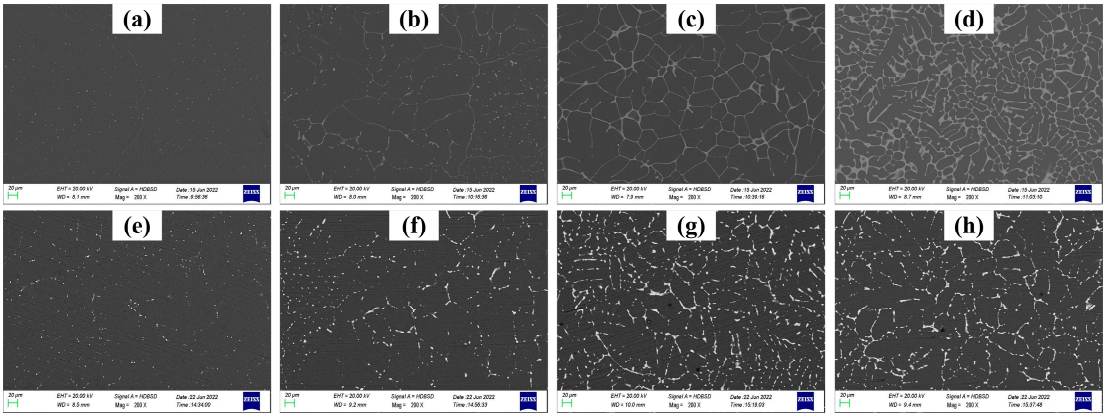


Figure 9. BSE scanning images of Mg-Ce binary alloys: (**a**–**d**) as-cast Mg-0.4Ce, Mg-1.0Ce, Mg-2.5Ce, and Mg-5.0Ce; (**e**–**h**) solution-treated Mg-0.4Ce, Mg-1.0Ce, Mg-2.5Ce, and Mg-5.0Ce.

Figure 10 presents the EDS analysis results for the ellipsoidal white second phase (point A) in the as-cast Mg-5.0Ce alloy. This EDS analysis of point A indicates that the continuous network-like second phase is rich in Ce, confirming that the ellipsoidal second phase is the Mg-Ce phase.

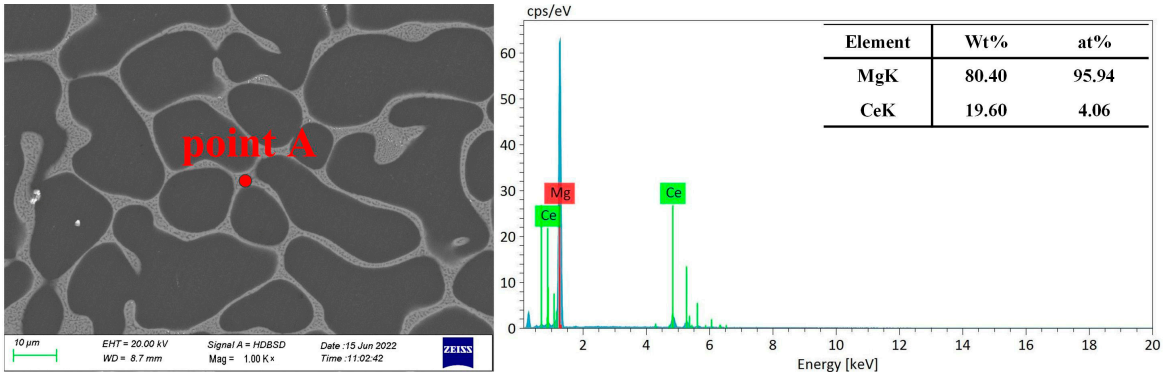


Figure 10. Energy spectrum analysis of as-cast Mg-5.0Ce.

The thermal conductivity of as-cast and solution-treated Mg-Ce binary alloys at room temperature is shown in Figure 11. As seen in the figure, the thermal conductivity of both

as-cast and solution-treated Mg-Ce binary alloys gradually decreases with increasing Ce content. As the Ce content increased from 0.2 wt.% to 5.0 wt.%, the thermal conductivity of the cast Mg-0.2Ce alloy decreased from 149.1 W/(m·K) to 126.4 W/(m·K). Concurrently, the thermal conductivity of the solution-treated Mg-0.2Ce alloy decreased from 155.8 W/(m·K) to 135.8 W/(m·K). Notably, the thermal conductivity of the solution-treated Mg-Ce binary alloy was higher than that of the corresponding cast Mg-Ce binary alloy.

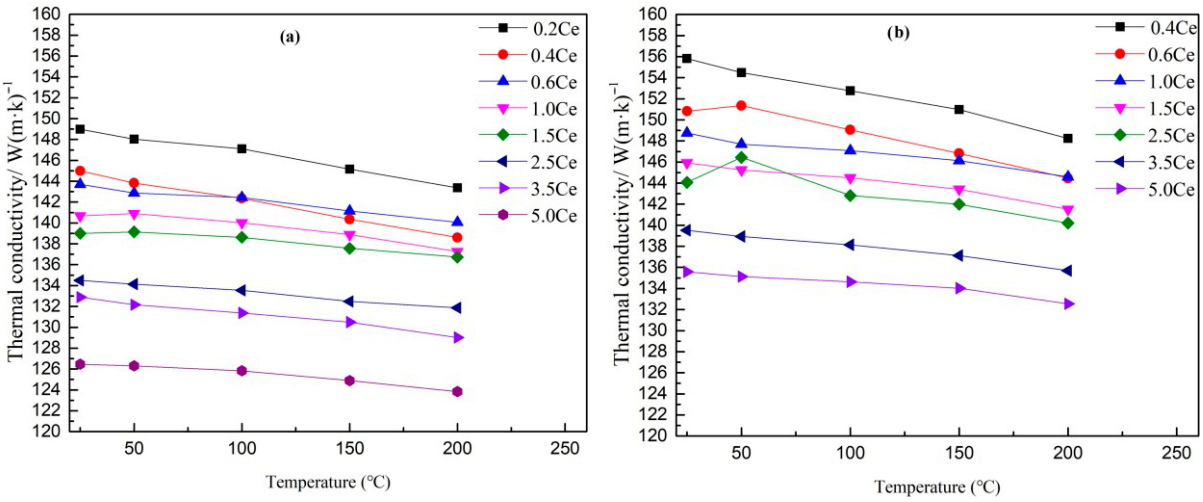


Figure 11. Thermal conductivity versus temperature curves of Mg-Ce alloy: (**a**) as-cast and (**b**) solution-treated.

In summary, the thermal conductivity of Mg-La(Ce) binary alloys after solution treatment is higher than that of as-cast Mg-La(Ce) binary alloys. On the one hand, the solubility of La(Ce) in the magnesium matrix is extremely low, with maximum solubility at the eutectic temperature being only 0.14 at.% (0.79 wt.%) and 0.09 at.% (0.52 wt.%). During solidification of the Mg-La(Ce) alloy, rapid cooling causes La(Ce) to become supersaturated in the magnesium matrix. In the subsequent solution treatment, the supersaturated La(Ce) elements precipitate out of the magnesium matrix, reducing the La(Ce) content in the matrix and thereby increasing the alloy's thermal conductivity. On the other hand, the relatively rapid cooling rate during solidification of the melted magnesium alloy leads to the generation of a large number of vacancies and dislocations. During the solution treatment, these lattice defects are reduced or eliminated to a certain extent. The reduction or elimination of lattice defects significantly contributes to the improvement of the thermal conductivity of magnesium alloys. Furthermore, as shown in Figures 4 and 8, solution treatment transforms the semi-continuous and continuous network compounds in the as-cast Mg-La(Ce) binary alloy into fine, dispersed particles distributed throughout the magnesium matrix. Compared to finely dispersed second-phase particles, semi-continuous and continuous network compounds severely impede electron and phonon conduction, thereby reducing the alloy's thermal conductivity. Consequently, it is evident from the above aspects that the thermal conductivity of Mg-La(Ce) binary alloys after solution treatment is higher than that of as-cast Mg-La(Ce) binary alloys.

3. Study on Heat Dissipation Properties of Mg-La(Ce)-Mn Ternary Alloys

3.1. Phase Diagram Study of Mg-Mn-La(Ce)Alloys

Research and development of materials, particularly the composition design of metallic materials, often relies on extensive experimental exploration to identify material compositions with favorable comprehensive properties. The advent of phase diagrams has introduced a novel approach to material composition design, providing a theoretical foun-

dation for seeking optimal compositions. By analyzing phase diagrams, solidification paths can be calculated to determine alloy-phase compositions, derive solubility data, and predict phase transformations. This enables the systematic determination of corresponding alloy compositions, thereby enhancing the systematic nature of alloy composition design [19].

To analyze the phase composition and solidification pathways of Mg-Mn alloys with varying La and Ce alloying elements, and to identify the composition ranges corresponding to target phase compositions, solidification pathway calculations were performed using Pandat_2021 software. This included both the equilibrium Lever model and the non-equilibrium Scheil model.

This project selected common alloying elements in magnesium alloys, including primary alloying elements Mg and Mn, along with rare earth elements La and Ce. The solidification paths for the primary alloying elements are shown in Figure 12. The Scheil solidification paths for the alloys in Figure 12a,b indicate that adding a small amount of the rare earth element Ce causes the CeMg12 phase to begin precipitating during the solidification process of the Mg-0.5Mn alloy. As the Ce content increases, the composition of the CeMg12 phase continues to rise. Simultaneously, the addition of Ce modifies the precipitation process of the Hcp phase: as Ce content increases, the liquid phase of the alloy rapidly decreases while the amount of Hcp phase precipitated increases.

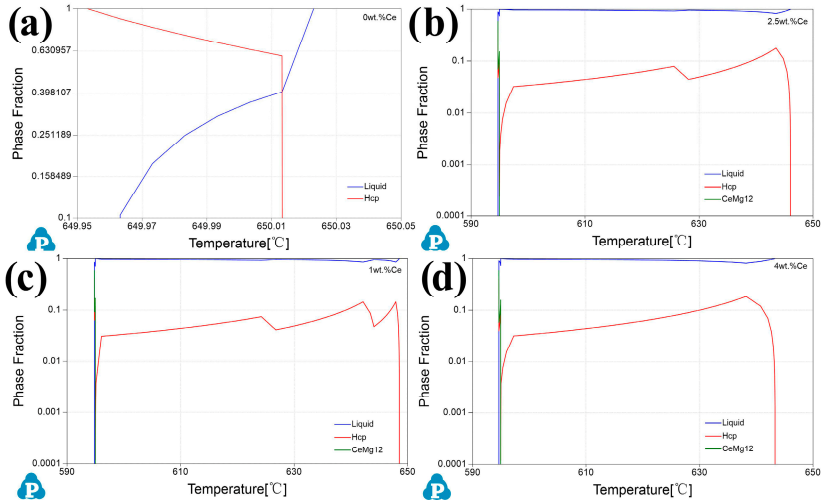


Figure 12. Phase diagram of Mg-0.5Mn-xCe ternary alloy: (**a**) 0.0 wt%Ce; (**b**) 2.5wt%Ce; (**c**) 1.0 wt%Ce; (**d**) 4.0wt%Ce.

3.2. Experimental Materials and Methods

Mg-Mn alloys, as early-developed commercial-wrought magnesium alloys, exhibit excellent extrudability and superior corrosion resistance, and this series offers moderate strength. Ce is the most commonly added rare earth element to magnesium alloys, serving to refine grain size and weaken the deformation texture of the alloy, thereby simultaneously enhancing both strength and formability.

The alloy design involves adding rare earth element Ce at mass fractions of 0.2%, 0.6%, 1.0%, and 2.0% to a Mg-0.5Mn base alloy. Raw materials include high-purity magnesium (99.98%), the Mg-20%Ce intermediate alloy, and Mn powder. These materials are melted in a low-carbon steel crucible under a mixed atmosphere (0.5 vol.% SF6 + 99.5 vol.% N2). The crucible was first preheated and dried. When the crucible temperature reached 200–300 °C, preheated pure magnesium ingots (200 °C) were added. Heating continued until the low-carbon steel crucible reached the target temperature of 750 °C. After complete melting of the pure magnesium ingots, the temperature was raised to 780–800 °C. Following removal of surface dross, magnesium-cerium intermediate alloy was added. Once fully melted,

manganese powder was introduced. The melt underwent dross removal and stirring. The temperature was then adjusted to 750 °C and held for 30 min. Finally, the melt was poured into a metal mold preheated to 300–350 °C, with dimensions of φ89 × 250 mm, and air-cooled to produce the desired ingot.

The specific composition of the alloy used in the experiment was tested using an X-ray fluorescence spectrometer, with the detailed composition shown in Table 4. Actual measurements of element contents are shown in parentheses; the alloy composition design is shown outside parentheses.

Table 4. Chemical composition of Mg-0.5Mn-xCe alloy.

Nominal Alloys	Compositions/wt.%		
	Ce	Mn	Mg
Mg-0.5Mn-0.2Ce	0.20(0.17)	0.50(0.53)	Bal.
Mg-0.5Mn-0.6Ce	0.60(0.52)	0.50(0.58)	Bal.
Mg-0.5Mn-1.0Ce	1.00(0.96)	0.50(0.72)	Bal.
Mg-0.5Mn-2.0Ce	2.00(1.91)	0.50(0.74)	Bal.

3.3. Microstructure and Thermal Conductivity of Mg-Ce-Mn Ternary Alloys

The SEM images of the as-cast Mg-0.5Mn-xCe alloy obtained by secondary electron scanning are shown in Figure 13. As seen in Figure 12a, for the as-cast Mg-0.5Mn-0.2Ce alloy, a small number of second-phase particles are distributed within the α-Mg matrix of coarse grains. When the Ce content reaches 0.6 wt.%, the dendrite arm spacing decreases, and a small amount of semi-continuous network compounds form. As the Ce content continues to increase, the volume fraction of the compounds rises, and they transform into a continuous network of compounds. Figure 14 presents EDS area scans and point energy-dispersive spectroscopy (EDS) results of the second phase in the as-cast Mg-0.5Mn-2.0Ce alloy. The spherical second-phase particles within grains (Spectrum 4) and the network compounds distributed along grain boundaries (Spectrum 1 and Spectrum 3) are primarily composed of Mg and Ce elements, with minor Mn content. Their specific chemical compositions, as shown in the EDS results of Figure 13, indicate that the second phases are rich in Ce. Spectrum 3 is distributed along grain boundaries. The specific chemical compositions, as shown in the energy spectrum results of Figure 13, indicate that the second phases are all rich in Ce. Spectrum 2, selected from within the grains, consists primarily of Mg and Mn with zero Ce content, demonstrating that Ce is enriched in second-phase particles within the grains and in the reticular compounds distributed along grain boundaries.

The temperature-dependent thermal conductivity curve of the as-cast Mg-0.5Mn-xCe alloy is shown in Figure 15a. As the temperature increases, the thermal conductivity of the as-cast Mg-0.5Mn-xCe alloy gradually rises. Mn and Ce atoms act as heterogenous solute atoms in the alloy. Their solid solution in the magnesium matrix causes severe lattice distortion and disrupts the periodicity of the lattice. As temperature increases, lattice vibrations intensify. Additionally, the frequency of electron–phonon and phonon–phonon collisions rises, both of which impede the free movement of electrons and phonons, reducing their mean free paths. However, the average velocity of electrons also increases with temperature. At higher temperatures, this effect becomes dominant, leading to a gradual increase in the alloy's thermal conductivity with rising temperature.

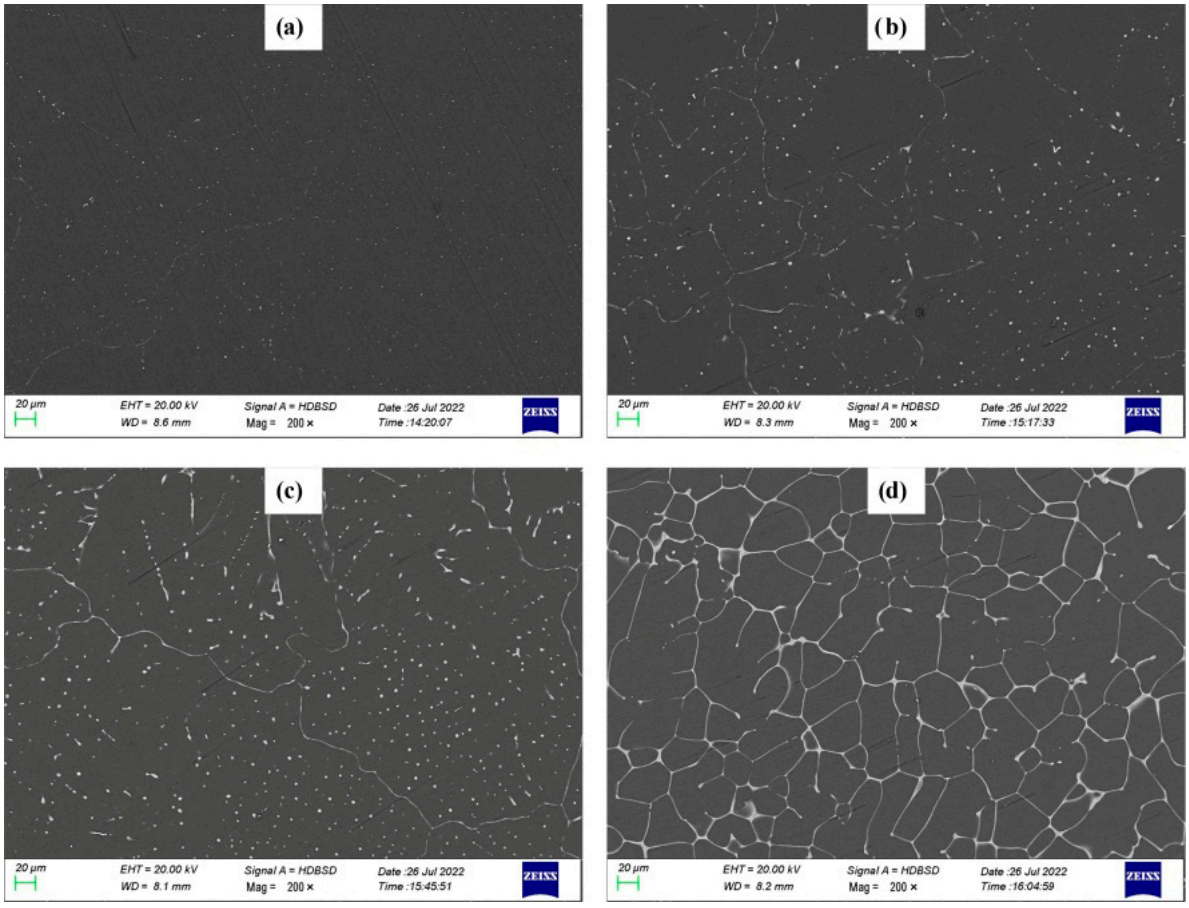


Figure 13. SEM scanning images of as-cast Mg-0.5Mn-xCe alloy: (**a**) x = 0.2; (**b**) x = 0.6; (**c**) x = 1.0; (**d**) x = 2.0.

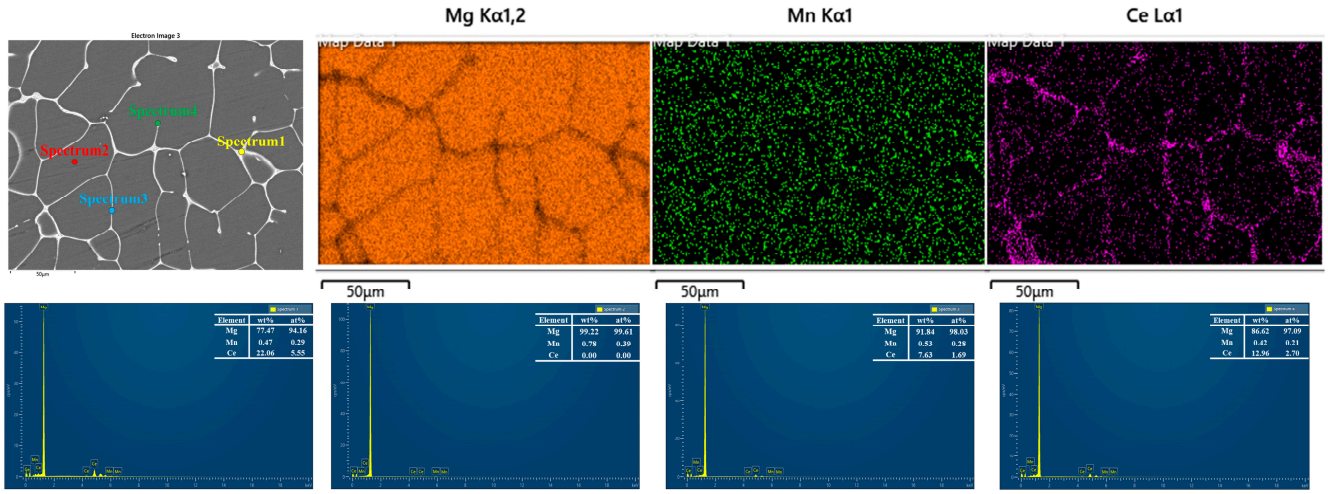


Figure 14. EDS surface scanning image and spectrum analysis results of secondary phase rich in Ce in as-cast Mg-0.5Mn-2.0Ce alloy.

Figure 15b shows the influence of Ce content on the thermal conductivity of as-cast Mg-0.5Mn alloys over the temperature range of 298–523 K. The thermal conductivities of as-cast Mg-0.5Mn-0.2Ce, Mg-0.5Mn-0.6Ce, Mg-0.5Mn-1.0Ce, and Mg-0.5Mn-2.0Ce alloys at room temperature are 125.6 W/(m·K), 121.5 W/(m·K), 115.6 W/(m·K), and 110.9 W/(m·K), respectively. The thermal conductivity data for Mg-0.2Ce in Figure 11 indicates that the addition of 5% Mn significantly reduces the alloy's thermal conductivity, decreasing from 149.1 W/(m·K) at room temperature to 125.6 W/(m·K), resulting in a reduction of 15.76%.

It is evident that the thermal conductivity of the as-cast alloys gradually decreases with increasing Ce content. When 0.6 wt.% Ce is added to the as-cast alloy, its thermal conductivity decreases by 4 W/(m·K). Upon further increasing the Ce content to 2.0 wt.%, the alloy's thermal conductivity drops to 110.9 W/(m·K). This occurs because the introduction of any alloying element into a metal disrupts the periodic integrity of the crystal lattice, interfering with the movement of free electrons and thereby reducing the alloy's thermal conductivity. As Ce content increases, the concentration of heterogenous solute atoms dissolved in the magnesium matrix gradually rises. This leads to greater lattice distortion in the magnesium matrix, increasing scattering of electrons and phonons and reducing their mean free path, thus lowering the alloy's thermal conductivity. Furthermore, as shown in Figure 13, the average grain size of the as-cast alloy progressively decreases with increasing Ce content, gradually forming continuous network compounds. Compared to discrete second-phase particles, these continuous network compounds severely impede electron and phonon conduction, reducing their mean free path. Consequently, under the combined influence of these factors, the thermal conductivity of the as-cast alloy gradually decreases with increasing Ce content.

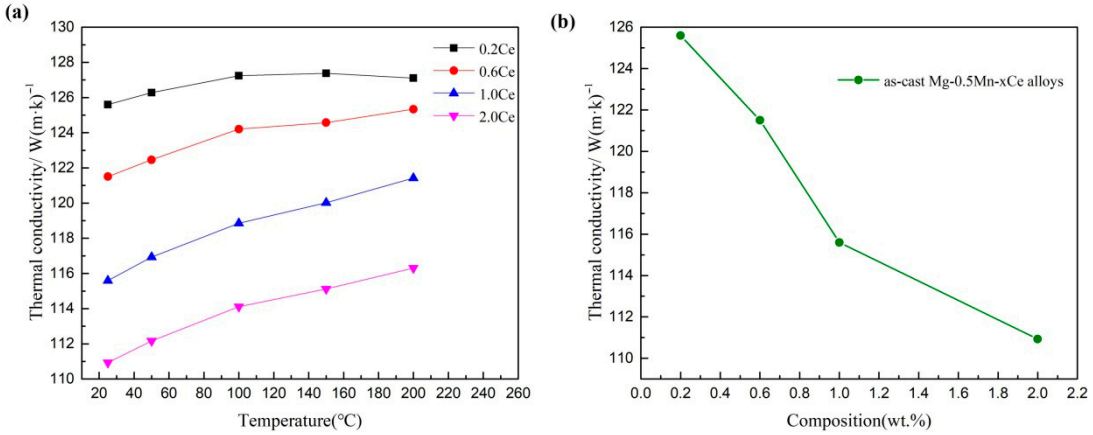


Figure 15. (**a**) Thermal conductivity versus temperature curves of as-cast Mg-0.5Mn-xCe alloy. (**b**) Thermal conductivity at room temperature versus Ce content curves of as-cast Mg-0.5Mn-xCe alloy (x = 0, 0.15, 0.3, 0.6).

4. Conclusions

1. Through CAFE simulation calculations, regulation can be achieved via the following methods: increasing the average nucleation undercooling, which leads to larger grain sizes; reducing the nucleation density, which results in larger grain sizes; and increasing the standard deviation of the average nucleation undercooling, which reduces the area of small grains while increasing the area of large grains.
2. The thermal conductivity of both as-cast and solution-treated Mg-La(Ce) binary alloys gradually decreases with increasing element addition. However, the thermal conductivity of solution-treated Mg-La(Ce) binary alloys is higher than that of as-cast alloys.
3. The addition of Ce helps refine the as-cast microstructure of Mg-0.5Mn alloys. As the Ce content increases, the volume fraction of the Mg12Ce phase also increases. The thermal conductivity of cast Mg-0.5Mn-xCe alloys gradually increases with rising temperature. Simultaneously, at room temperature, the thermal conductivity of cast Mg-0.5Mn alloys decreases gradually with an increasing Ce content. This decrease slows progressively due to the precipitation of the Mg12Ce phase.

Author Contributions: Conceptualization, W.H. (Wei He) and W.H. (Wenxin Hu); methodology, Y.L. (Yuming Lu); software, K.L.; validation, B.K.; formal analysis, S.Q.; investigation, F.L.; resources, W.W.;

data curation, W.H. (Wei He); writing—original draft preparation, W.H. (Wei He); writing—review and editing, W.H. (Wei He); visualization, Y.L. (Yuan Li); supervision, Z.L.; project administration, H.G.; funding acquisition, W.H. (Wei He). All authors have read and agreed to the published version of the manuscript.

Funding: Open Subject of Rare Earth New Material Technology Innovation Center (Project Name: Study on Microstructural Transformation Mechanisms and Corrosion Resistance of LPSO-Phase-Containing Mg-Y-Zn Alloys: Applications and Development; Project Number: G2025-K-11(18)-33(55)).

Data Availability Statement: The original contributions presented in this study are included in the article. Further inquiries can be directed to the corresponding author.

Conflicts of Interest: Authors Bin Kang and Siyuan Qu were employed by the company Inner Mongolia Northern Rare Earth Advanced Materials Technology Innovation Co., Ltd. The remaining authors declare that the research was conducted in the absence of any commercial or financial relationships that could be construed as a potential conflict of interest.

References

1. Cong, W.; Wang, F.; Du, X.; Wang, Z.; Zhou, L.; Wei, Z.; Mao, P.; Li, J. Study on Microstructure, Mechanical Properties and Thermal Conductivity of Vacuum-Assisted High Pressure Die Casting Mg-5Zn-xCu-0.5Zr Alloy. *Mater. Sci. Eng. A* **2025**, *938*, 148478. [CrossRef]
2. Han, J.; Bai, Y.; Zhang, X.; Wang, G.; Zhao, D.; Cheng, W.; Teng, X. Understanding the Mechanisms of Thermal Conductivity in Mg-Zn-Ca Alloys with Multi-Component Second Phases. *Mater. Today Commun.* **2025**, *46*, 112545. [CrossRef]
3. Liang, T.; Chen, T.; Wang, J.; Zhang, L.; Wu, L.; Chen, X.; Wang, J.; Yuan, Y. The Correlation between Electrical Conductivity and Thermal Conductivity of Binary Mg Alloys. *J. Alloys Compd.* **2025**, *1035*, 181553. [CrossRef]
4. Bai, G.; Li, J.; Yan, Y.; Wang, Y.; Tang, S. Enhancing the Thermal Conductivity of Mg/Diamond Composites Prepared by Gas Pressure Infiltration through Zr Coating and Heat Treatment. *Colloids Surf. A Physicochem. Eng. Asp.* **2025**, *719*, 137060. [CrossRef]
5. Chen, L.; Wang, M.; Guo, W.; Li, J.; Lü, S.; Guo, W.; Wu, S. Synthesis and Molecular Dynamics Investigation of Mg/SiCP Composites with High Thermal Conductivity and Low Expansion. *J. Magnes. Alloys* **2025**, *in press*. [CrossRef]
6. Duan, S.; Zhou, X.; Mo, L.; Chen, L.; Du, J. Significant Ductility Enhancement for High Thermal Conductivity Mg-2Sn-2.3La Alloy via Zn Addition. *Mater. Sci. Eng. A* **2024**, *916*, 147343. [CrossRef]
7. Fan, J.; Yang, Q.; Lv, S.; Meng, F.; Gu, H.; Zhang, J.; Cheng, Y.; Li, R.; Qiu, X. Synergetic Tensile Properties and Thermal Conductivity of High-Pressure Die Casting Mg-Al-RE Alloys Controlling by Various Al and La Additions. *J. Alloys Compd.* **2025**, *1032*, 181121. [CrossRef]
8. Li, X.; Wang, T.; Du, W.; Lou, F.; Ren, J.; Du, X.; Liu, K.; Li, S.; Wang, Z. Unveiling the Roles of Zn Content on the Thermal Conductivity of Mg-8Gd-1Er-xZn-1Mn Alloys. *J. Mater. Res. Technol.* **2025**, *35*, 6804–6813. [CrossRef]
9. Liao, Q.; Wang, Z.; Hu, W.; Le, Q.; Yan, H.; Nan, X. Effect of Solid Solution and Precipitation on Thermal Conductivity and Mechanical Properties of Mg–Zn–Cu–Ce Magnesium Alloy. *J. Mater. Res. Technol.* **2025**, *35*, 5923–5932. [CrossRef]
10. Shang, Q.; Dong, Q.; Tan, J.; Lv, H.; Wang, F.; Wu, G.; Yu, P.; Jiang, B.; Tang, A.; Pan, F. Synergistic Enhancement of Thermal Conductivity and Mechanical Properties in Cast Mg-Zn-Zr-Sr Alloys via Grain Refinement and Solute Redistribution. *J. Alloys Compd.* **2025**, *1036*, 182094. [CrossRef]
11. Wang, F.; Jiang, J.; Bi, G.; Lu, X.; Meng, S.; Li, Y.; Chen, T. Effects of Al Addition on Microstructure, Mechanical Properties and Thermal Conductivity of an Extruded Mg-Y-Zn-Co Alloy. *Mater. Today Commun.* **2025**, *46*, 112499. [CrossRef]
12. Xing, Y.; Luo, J.; He, Q.; Cheng, Y.; Xin, Y. An Mg-1Zn-1Cu-xCe Alloys with Both High Ductility and High Thermal Conductivity. *J. Alloys Compd.* **2025**, *1025*, 180247. [CrossRef]
13. Liu, H.; Yang, X.; Zhang, Y.; Nagaumi, H.; Zhao, M.; Shi, Z.; Atrens, A. Simultaneous Enhancement of Strength and Thermal Conductivity of Extruded Mg−Mn−Zn Alloy via Hot Compression. *Trans. Nonferrous Met. Soc. China* **2025**, *35*, 819–831. [CrossRef]
14. Liu, H.; Nakata, T.; Xu, C.; Tang, G.; Li, D.; Wang, X.; Wang, G.; Kamado, S.; Geng, L. Effects of La and Ce on the Microstructure, Thermal Conductivity and Strength Synergy of the as-Extruded Mg-Mn-RE Alloys. *J. Magnes. Alloys* **2025**, *13*, 654–667. [CrossRef]
15. Jiang, C.; Shao, D.; Liang, J.; Zhang, Y. Decoding the Annealing Treatment-Microstructure-Thermal Conductivity Nexus in Heterogeneous Mg-Mn-Ce Alloy. *J. Mater. Res. Technol.* **2025**, *38*, 5757–5767. [CrossRef]
16. Hui, S. Compositional Design of Mg-Ce/La-Zn Heat Dissipation Alloy Aided by Thermodynamic Calculations. Master's Thesis, Shanghai University, Shanghai, China, 2020.
17. Miao, F.; Xie, L.; Li, J.; Tian, R.; Wang, R.; Kang, Y.; Yan, Z. Evolution of Solidification Structure of Cu-3Ni-0.96Si-0.15Mg Alloy Ingot Based on CAFE Simulation. *Hot Work. Technol.* **2024**, *53*, 135–140. [CrossRef]

18. Cui, X.; Li, F.; Ma, J.; Zhang, Q. CAFE Simulation of Solidification Structure of Ti-6Al-4V Titanium Alloy. *Spec. Cast. Nonferrous Alloys* **2024**, *44*, 717–720. [CrossRef]
19. Tian, Y. Phase Diagram Determination of Mg-Zn-Sm-Mn System and Study on Thermal Conductivity and Mechanical Properties of Its Alloys. Doctoral Dissertation, Shanghai University, Shanghai, China, 2023.

Disclaimer/Publisher's Note: The statements, opinions and data contained in all publications are solely those of the individual author(s) and contributor(s) and not of MDPI and/or the editor(s). MDPI and/or the editor(s) disclaim responsibility for any injury to people or property resulting from any ideas, methods, instructions or products referred to in the content.